Mixed Molybdenum–Tungsten Oxide as Dual-Band, VIS–NIR Selective Electrochromic Material

Florian Gillissen, Michaël Lobet, Jennifer Dewalque, Pierre Colson, Gilles Spronck, Rachel Gouttebaron, Mathieu Duttine, Brandon Faceira, Aline Rougier, Luc Henrard, Rudi Cloots,* and Anthony Maho*

The energy efficiency of smart windows can be greatly improved by integrating dual-band electrochromic materials based on nanostructured doped metal oxides, as these allow for the dynamic and independent control of light and heat supplies in buildings, respectively, related to transmitted visible (VIS) and near-infrared (NIR) solar radiations. Mixed molybdenum–tungsten oxides $Mo_yW_{1-y}O_{3-\delta}$ "MoWOx" are considered as innovative compounds in this context: in comparison with parent $WO_{3-\delta}$ formulations, a remarkable increase of unpaired electrons can be obtained from the formation of a larger amount of both reduced species and oxygen vacancies during the synthetic process of MoWOx materials, with a consequently boosted intensity of light absorption by 850–900 nm wavelengths. Consecutively, spin-coated films obtained from MoWOx structures, solvothermally synthesized for 1 h from 2/1 Mo/W atomic ratios, are shown to be electrochromically commutable through a noticeable VIS-darkened and NIR-transparent warm state, while $WO_{3-\delta}$ benchmarks classically evolve between bright (VIS- and NIR-bleached), cool (VIS-bleached, NIR-opaque), and dark (VIS- and NIR-opaque) states. All in all, such advanced optical functionalities are of high interest for fine-tuning the selectivity and improving the efficiency of electrochromic fenestration solutions, further improving their capacity to adapt to different climates, seasons, and user preferences.

1. Introduction

Nanostructured heavily doped semiconductors testify for near-infrared (NIR) optical absorption through localized surface plasmon resonance (LSPR) phenomena, in which the free charge carriers collectively oscillate upon interaction with incident electromagnetic radiation.[1–3] The plasma frequency ω_p of the materials depends directly on the quantity of these free charge carriers, as well as on other parameters such as the particle size, shape, composition, and environment.[1,4] Therefore, their optical absorption can be tuned by varying the free charge carrier concentrations between values from 10^{19} to 10^{21} cm^{-3}, specifically by means of synthetic doping. Different strategies have been developed accordingly to tune the optical response in tungsten-oxide (WO_3)-based compounds, including the formation of bronzes by heteroatom doping with Li, Na, K, Rb, Cs, etc.,[5–7] or via the creation of oxygen vacancies, and therefore of substoichiometric $WO_{3-\delta}$ formulations, especially by means of solvothermal treatment[8–13] or synthesis under controlled atmosphere (typically using Schlenk line setups).[14–16]

Given their capacity to selectively modulate NIR light absorption, such electronically tunable nanomaterials are highly interesting for electrochromic applications, in which optical modulation is controlled postsynthesis by applying an appropriate electrochemical bias.[1] Typically, $WO_{3-\delta}$ compounds have been explored to induce an electrochromic behavior in the 800–1300 nm region, which accounts for nearly half of the infrared intensity of an incoming solar source.[2,4] The origin of this absorption at energies much smaller than the bandgap is still questioned, but often associated with the additional electrons brought either by the ionization of the dopant species, or liberated during the formation of oxygen vacancies.

According to various authors, NIR optical properties of the then-created degenerate semiconductor nanocrystals are ruled by the free electron density in the conduction bands and the associated LSPR resonance, while the visible (VIS) response is driven

F. Gillissen, J. Dewalque, P. Colson, G. Spronck, R. Cloots, A. Maho
Group for Research in Energy and Environment from Materials (GREEnMat)
University of Liège
Quartier Agora - B6a, Allée du Six-Août 13, Liège 4000, Belgium
E-mail: rcloots@uliege.be; anthony.maho@icmcb.cnrs.fr

M. Lobet, R. Gouttebaron, L. Henrard
Department of Physics
Namur Institute of Structured Matter
University of Namur
Rue de Bruxelles 61, Namur 5000, Belgium

M. Duttine, B. Faceira, A. Rougier, A. Maho
University of Bordeaux
CNRS
Bordeaux INP
ICMCB
UMR 5026, 87 Avenue du Dr Albert Schweitzer, Pessac 33600, France

**ADVANCED
SCIENCE NEWS**

www.advancedsciencenews.com

**ADVANCED
OPTICAL
MATERIALS**

www.advopticalmat.de

by polaronic phenomena and responsible for its "conventional" electrochromism.[4,17] On one hand, if the additional electrons are not associated with electronic states localized near vacancies whose energies lie within the bandgap, they are delocalized into the conduction band of the oxide, without reduction of the transition metal atoms;[18] consequently, a plasmonic optical response is expected in the case of nanocrystalline compounds. On the other hand, if the newly added electrons occupy localized states having energies within the bandgap, the metallic tungsten (W) atoms are partly reduced to W^{5+}, as reported in literature from X-ray photoelectron spectrometer (XPS) measurements,[19,20] and therefore, no plasmonic response is expected. The latter situation is often referred to as a polaronic effect, even though it is rather similar to a color center phenomenon,[21] which is different from the polaron met in the trivalent oxides – nevertheless, this terminology is used in the present study so to be consistent with the literature. It has also been shown that, upon further doping by alkali atoms, the extra electrons occupy states localized on the vacancy sites,[22] in line with the polaronic hypothesis. The absence of a consensus on this matter is also due to the numerous crystalline phases of the considered nanocrystals, highly depending on the synthesis conditions and the charge states.[23] Indeed, the vacancy states have been shown to depend on the phase and, for each phase, on the crystallographic site of the missing oxygen atoms. Up to now, simulations have not been conclusive on the role of the vacancy states because of the strong dependence of the results on the functional in DFT calculations.[24]

Beyond this ongoing debate on the fundamentals of their optoelectronic behavior, these semiconducting materials have a concrete applied use in allowing a so-called *dual-band* VIS–NIR electrochromic modulation behavior,[1,2,4,17] in which three states of optical filtration are generally available: the conventional *bright* and *dark* states (respectively, transparent and opaque in both VIS and NIR), and an intermediate, NIR-selective, *cool* state (VIS-transparent and NIR-dark).[2] Therefore, electrochromic fenestration solutions being designed and operated upon this dual-band system could improve the energy efficiency of smart windows and exceed the energy savings already reached by conventional electrochromic technology,[25,26] owing to a more efficient, selective control over the transmitted visible (luminosity) and NIR (heat) contributions of the solar radiations in buildings.

Even though dual-band materials offer an innovative functionality in comparison to their conventional counterparts, they still suffer from some limitations, preventing them from large scale production and widespread implementation. Solutions for circumventing these issues have been proposed in previous works of the literature, among those: the improvement of their selectivity toward the VIS and NIR ranges,[27,28] the development of suitable counter electrodes to improve the selectivity and efficiency of electrochromic devices,[1,17] the use of conductive substrates with broadband transparency as to not impair with the electrochromic behavior of the material (particularly in the NIR),[17] as well as the getting of a fourth, *warm* filtration state (VIS-dark and NIR-transparent) so to further improve the functionality and efficiency of the devices.[27–31]

In a will to optimize the degree of NIR/VIS selectivity in tungsten-oxide-based electrochromic materials, molybdenum−tungsten mixed oxides have been identified as interesting candidates. The association of molybdenum with (stoichiometric) WO_3 compounds has already been reported to improve their conventional (i.e., nonplasmonic) electrochromic performances by improving coloration efficiency, contrast between optical states, stability, reversibility, and durability of the material, or by yielding a more neutral color in the dark state.[32–45] Among those, several works have proven the efficiency of molybdenum (Mo) doping, with the doped formulation exhibiting enhanced properties in all key performance indicators (contrast, kinetics, coloration efficiency, and durability), and more specifically in the case of 2 at% Mo, displaying the best results, as shown by Zhou et al. in 2016[32] or by Wang et al. in 2018.[37] Besides, Li et al. have also demonstrated the possibility to obtain good electrochromic performances by substituting a larger amount of W, thus described as hybridization or mixing instead of doping.[40–42,45] However, to this day, none of these studies have highlighted neither NIR-selective behavior, nor dual-band functionality from these formulations. On the other hand, the concomitant formation of the mixed oxide as well as oxygen vacancies could lead to a further increased concentration of free charge carriers, being necessary to support LSPR features and to display a dual-band electrochromic behavior. As a matter of facts, several works have already highlighted the occurrence of a plasmonic behavior in such oxygen-deficient molybdenum−tungsten mixed oxides,[8–12,46–48] showing a large increase in their optical signature in comparison to the $MoO_{3-\delta}$ and $WO_{3-\delta}$ parent formulations, and accounting for a 15–20 times increase in absorption, respectively.[8] However, the current state of the art focusing on these molybdenum−tungsten mixed oxides has only addressed catalytic and optoelectronic applications so far, such as hydrogen evolution reaction,[10,11] photocatalysis,[8,47] surface-enhanced Raman spectroscopy,[9] and NIR shielding.[46] The NIR absorption ability of this material, coupled with the electrochromic activity expected from selected plasmonic materials, therefore appears as extremely promising for the use of mixed **Mo–W Ox**ide formulations (labeled as "MoWOx) compounds as dual-band electrochromic materials.

In the perspective of designing novel electrochromic materials, the combination of both oxygen vacancy doping (to allow the support of plasmonic features) and molybdenum incorporation (to improve the VIS electrochromic performances of WO_3) bears great potential for enhancing the selective electrochromic modulation of VIS and NIR ranges, as shown hereafter, which has never been reported before, to the best of our knowledge.

The present contribution aims at the efficient synthesis of suitable mixed MoWOx formulations, and their deposition as films through wet coating approaches. The combined impact of the Mo–W mixing and of the formation of additional oxygen vacancies on the morphological, crystalline, and more importantly optical and electronic properties of the materials, is carefully investigated in order to assess their potential as dual-band electrochromic material, specifically in terms of VIS/NIR selectivity, coloration and bleaching behavior, and reversibility.

2. Results

2.1. Solvothermally Synthesized "MoWOx" and WO$_{3-\delta}$ Powders

2.1.1. Preliminary Rationalization of the Synthetic Parameters: Mo/W Stoichiometry and Duration of the Solvothermal Process

Different formulations of MoWOx mixed oxides have been synthesized through a one-step solvothermal process on the basis of a reported protocol.[8] As starting compounds, three Mo/W molar ratios (2/1, 1/1, and 1/2) are selected, while other synthetic parameters are maintained identical: i.e., a 160 °C temperature and a 12 h duration.

Optical measurements in undiluted conditions (see absorption spectra in Figure S1, Supporting Information), reproducing previous literature,[8,10,46,47] as well as in 10 wt% diluted conditions (see inset in Figure S1, Supporting Information) in order to meet the requirements of the Kubelka–Munk (KM) formalism[48] (cf. the Experimental Section), show that the MoWOx 2/1 sample presents the most intense absorption properties out of the three ratios. Displaying a maximum at the beginning of the NIR, namely in the 800−1300 nm range where most of the NIR solar radiative intensity is found, this particular MoWOx formulation confirms its interesting potential as dual-band, VIS, and NIR active electrochromic material. The remainder of this work will therefore focus on the investigation of this formulation and the characterization of its properties.

The impact of synthesis duration is then investigated, probing the evolution of the morphological, structural, optical, and electronic properties of the material as the particles grow in the solvothermal reactor, with syntheses carried out during 1–12 h. For all durations, urchin-like particles are obtained with a solid core covered by an outer layer of nanorods, growing from an average of 1.5 ± 0.5 µm at 1 h to 2.6 ± 0.6 µm after 3 h and up to 12 h (see scanning electron microscopy SEM images and Energy Dispersive X-Ray EDX analyses in Figure S2, Supporting Information). The urchin-like MoWOx particles do not grow further after 3 h of solvothermal treatment, but the size dispersion of the particles appears to decrease as the duration of the solvothermal process increases, indicating a homogenization of the morphological properties of the urchin-like particles and a more robust protocol (Figure S2, Supporting Information). Given the narrower dispersion found after 12 h, and with the latter also being the duration studied in previous works of the literature,[8,9,12,47] only 1 and 12 h durations are selected in the frame of this work. In addition to the two MoWOx formulations (2/1, 1 and 12 h), two WO$_{3-\delta}$ parent oxides produced following the same synthetic protocols (160 °C, 1 and 12 h) are also considered as benchmark formulations, and accordingly synthesized and characterized. The samples obtained from the solvothermal process exhibit different colorations (see pictures shown in Figure S3, Supporting Information), notably: a dark blue tint in the case of both 1 and 12 h MoWOx formulations, while the WO$_{3-\delta}$ parent oxides display lighter colors, with the 1 h sample leaning toward a gray/green color and its 12 h counterpart being recovered as a light gray powder. Noteworthy, parent MoO$_{3-\delta}$ formulations are not considered in details in the present study, as preliminary trials have shown that the obtained particles are not stable enough to be processed as suspensions for thin film deposition, forming a thick slurry unable to be de-posited by spin coating when prepared in the same conditions as the other formulations (125 mg mL^{-1} in ethanol, see the Experimental Section). Still, the main morphological, structural, and optical properties of this formulation are presented in Figure S4 (Supporting Information).

2.1.2. Morphological and Structural Analysis of "MoWOx" 2/1 and WO$_{3-\delta}$ Powders

Transmission electron microscopy (TEM) images of the four formulations of interest are presented in **Figure 1**, displaying very different morphologies. In the case of the MoWOx particles, both formulations highlight an urchin-like morphology, with the 1 h formulation (Figure 1A, 1.5 ± 0.5 µm) growing into its larger 12 h counterpart (Figure 1B, 2.6 ± 0.6 µm). However, due to the dense packing of nanorods at the surface of the urchins, the core-to-nanorods ratio could not be monitored nor tuned as a function of the time under solvothermal treatment from these measurements. For the parent WO$_{3-\delta}$ formulations, the morphology varies significantly as a function of the time, evolving from aggregated nanospheres (6.4 ± 1.6 nm) in the case of WO$_{3-\delta}$ 1 h (Figure 1C), to micrometric hexagonal platelets ($L \times W \times H = 1.9 \times 1.9 \times 0.2$ µm ($\pm 0.4 \times 0.1 \times 0.1$ µm)) after 12 h of solvothermal treatment (Figure 1D). Importantly, the nanostructures found in these materials − i.e., either the nanospheres (Figure 1C), the nanometric thickness of the hexagonal platelets (Figure 1D), or the nanorods at the surface of the urchins (Figure 1A,B) − can allow the support of plasmonic features in these formulations.

In addition, high-resolution TEM imaging is carried out on the four materials to further evaluate their structural properties, presented in Figure S5 (Supporting Information). In both MoWOx cases (Figure S5A,B, Supporting Information), the microscopy images of the nanorods at the surface of the urchins show the presence of crystalline zones exhibiting fringes perpendicular to the orientation of the nanostructure. However, even if the crystallites in a given nanorod appear to all be oriented in the same direction, the electronic diffraction pattern appears as a ring, since the surface of the urchins is made of numerous nanorods oriented in all directions. The two MoWOx formulations exhibit interplanar distances of 3.7 Å, in good accordance with the interplanar distance of previously reported Mo-doped monoclinic W$_{18}$O$_{49}$.[9–12] Besides, WO$_{3-\delta}$ 1 and 12 h (Figure S5C,D, Supporting Information) display clearly defined hexagonal fringes, which could be expected from the hexagonal morphology of the platelets: measurements result in an interplanar distance of 3.5 Å and angles of 60° between the three planar orientations. This observation is completed by the electronic diffraction spot pattern, indicating the presence of large and well crystallized grains in the 12 h sample (Figure S5D, Supporting Information).[43] A similar signal is also observed in WO$_{3-\delta}$ 1 h (Figure S5C, Supporting Information), although at weaker intensity: given the smaller dimensions of the particles, the growth of the crystallites is also limited and the electronic diffraction appears as less intense.

Complementary EDX characterization of the MoWOx powders (achieved in the SEM experimental setup, see Figure S2 in the Supporting Information) highlights a disparity in the Mo/W ratios, with a molybdenum rich oxide for short-duration
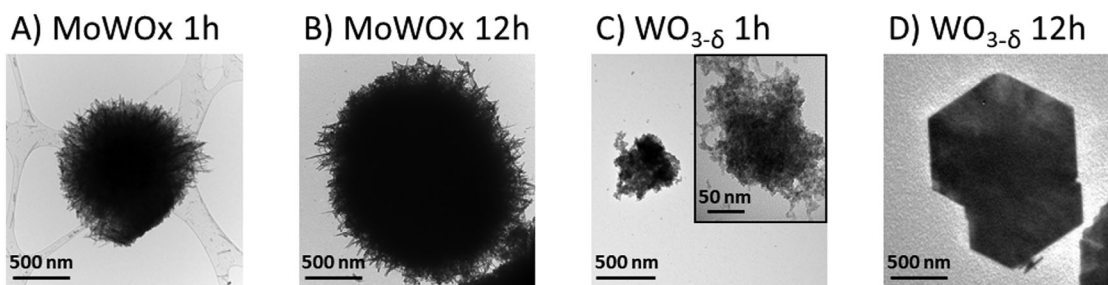
Figure 1. TEM images of particles of A) MoWOx 1 h, B) MoWOx 12 h, C) $WO_{3-\delta}$ 1 h (with a greater magnification on an aggregate in inset), and D) $WO_{3-\delta}$ 12 h.

synthesis (Mo/W = 5/1 for the 1 h case), followed by a decrease in the relative Mo content over longer durations (3 h and more) to finally attain the targeted ratio of 2/1 (the initial ratio of precursors in the reactive medium, see the Experimental Section). These results tend to indicate faster reaction kinetics for the molybdenum species in comparison to the tungsten ones, leading to the formation of Mo-rich particles first, to which the remaining dissolved tungsten incorporates over the next hours of reaction, until the reactive medium is completely depleted from metallic precursors.

X-ray diffraction (XRD) characterization of the MoWOx powders (**Figure 2**) exhibits only two diffraction peaks at 22.7° and 46.4°, respectively, indexed as the (010) and (020) planes of a monoclinic $W_{18}O_{49}$ nanowire pattern (PDF 04-005-4314; cell constants: $a = 18.32$ Å, $b = 3.79$ Å, and $c = 14.04$ Å). The presence of only two peaks in the same diffraction axis can be correlated to an anisotropic growth of the crystallites alongside the longitudinal axis of the nanowire. Given the preferential growth of nanorods at the surface of the MoWOx particles and the diffractograms obtained from these samples, it seems that these outer nanorods are mainly responsible for the crystallinity in the mixed formulations. Since molybdenum-rich oxides are obtained at short reaction time, and no molybdenum oxide signature is observed in the diffractograms, it would indicate that the core of the urchins (containing most of the Mo, see EDX discussion above) is mainly

amorphous, as indicated from the broad signals between 25° and 35° and between 45° and 60°. In addition, the EDX cartography of a MoWOx 1 h particle (Figure S6, Supporting Information) shows a homogeneous distribution of the different elements in the core of the urchins, with no formation of large $MoO_{3-\delta}$ segregated grains. Consequently, the diffractograms are interpreted as showing that only the outermost layer of nanorods contains $WO_{3-\delta}$-rich crystallites, while the center of the urchins consists in homogeneous Mo-rich amorphous material (for which of course no clear sharp signal is detected in the samples). Besides, the two $WO_{3-\delta}$ compounds can be indexed as a hexagonal WO_3 diffraction pattern (PDF 04-007-2322), with the difference that $WO_{3-\delta}$ 1 h only exhibits part of the diffraction peaks, with weak and broad diffraction signals visible at 23.0°, 28.2°, 36.7°, 50.0°, and 55.7° corresponding to the (001), (200), (201), (220), and (202) planes, respectively. The low crystallinity presented by this sample is probably due to the nanometric dimensions of the particles (limiting the crystallite size range that can be reached during the growth of the particles, measured at 30 nm using Scherrer equation), while the larger $WO_{3-\delta}$ 12 h hexagonal platelets can further crystallize during the longer solvothermal treatment they undergo (with an average crystallite size of 49 nm).

2.1.3. Optical and Electronic Analyses of "$MoWO_x$" 2/1 and $WO_{3-\delta}$ Powders

The KM optical characterization of the powders diluted in lithium fluoride (LiF, 10 wt%, **Figure 3**) shows a strong increase in the absorption of the Mo–W mixed oxide formulations in comparison to parent $WO_{3-\delta}$ ones, as expected from previous studies,[8,47] but also a more intense absorption signal in both $WO_{3-\delta}$ 1 h and MoWOx 1 h than for their 12 h counterparts. Furthermore, the absorption signature of MoWOx samples could be interpreted as a superposition of polaronic and plasmonic absorption signals, as previously reported in the literature.[6,46,49] Based on a graphical deconvolution of the signals (see Figure S7 in the Supporting Information), the optical signature of MoWOx 1 h consists of two contributions, with a first peak centered at 750 nm (corresponding to the polaronic behavior), and a second one at 1350 nm (related to the plasmonic absorption). When synthesized in the same conditions, the plasmonic response of $WO_{3-\delta}$ lies at 1500 nm (Figure 3, solid red line) in good accordance with previous reports.[48] Upon mixing with Mo, it is expected for numerous oxygen vacancies to be created in the material, leading
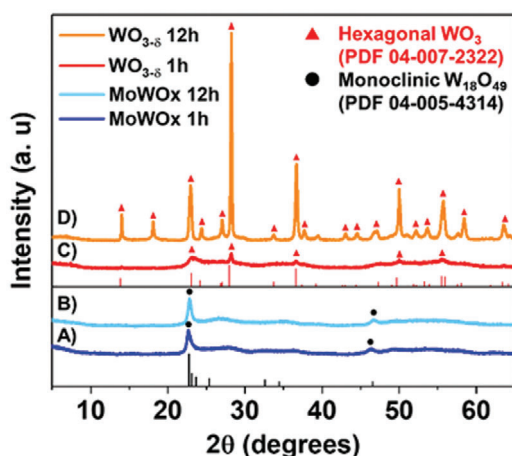

Figure 2. XRD diffractograms of A) MoWOx 1 h, B) MoWOx 12 h, C) $WO_{3-\delta}$ 1 h, and D) $WO_{3-\delta}$ 12 h powders. The diffraction scans are stacked at regular intervals of 100 counts.
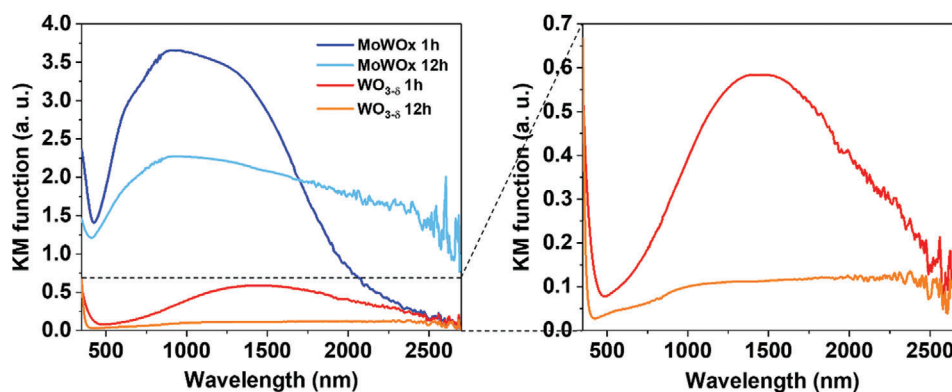
ADVANCED
SCIENCE NEWS

www.advancedsciencenews.com

ADVANCED
OPTICAL
MATERIALS

www.advopticalmat.de

Figure 3. KM function obtained from diffuse reflectance data of the MoWOx 1 h, MoWOx 12 h, $WO_{3-\delta}$ 1 h, and $WO_{3-\delta}$ 12 h powders (all being diluted in a 100/10 LiF/sample ratio).

to an increase in free charge carriers, and the ensuing blueshift of the plasmonic response observed from the parent oxide to the mixed formulation. Moreover, MoWOx 12 h exhibits two peaks at 820 and 1900 nm, with the strong redshift of the plasmonic signal being potentially due to the larger dimensions of the particles and to a reduction of the electronic density in the conduction bands, on which the LSPR frequency depends.[1,3,50,51] This shift toward higher wavelengths results in a large decrease in intensity and a broadening of the signal for the $MoWO_x$ 12 h, stretching over a larger region of the spectrum, in comparison to the better defined peak observed for $MoWO_x$ 1 h. The superposition of the polaronic and plasmonic contributions, probably arising from the increase in both reduced species and free charge carriers, results in an enhanced absorption of the two $MoWO_x$ powders with a maximum in absorption localized in the range of 850–900 nm. For the $WO_{3-\delta}$ parent oxides, the signal is interpreted as a single contribution at 1470 nm in the 1 h case: it is believed to correspond to a plasmonic resonance from selected literature[6,46,49] while being also consistent with a polaronic signature of thin films,[52] reminiscent of the lack of consensus on the dual-band charge/discharge model (as discussed in the Introduction). Meanwhile, no apparent peak is observed for $WO_{3-\delta}$ 12 h.

Given the optical results in Figure 3, an increased number of oxygen vacancies and reduced species are likely formed in the mixed formulations, and specifically at the beginning of the solvothermal treatment (with greater absorption signals in the 1 h samples compared to the 12 h ones). This may owe to the nature of the isopropanol solvent (being a proton donor and reducing agent[53,54]), potentially leading to the insertion of H+ in the crystal lattice, and therefore of the associated electrons (either free or localized over W^{5+} and Mo^{5+} species) to retain the charge neutrality. In addition, the substitution of Mo in the WO_3 octahedral sites of the MoWOx (and vice versa of W in the MoO_3 sites) could induce the formation of strains and defects, consecutively modifying the electronic and optical properties by creating color center (or polaronic) states and changing the bandgap of the material.[8,55,56] As a consequence, the synergistic formation of both reduced species and free electrons, originating from the creation of oxygen vacancies, can lead to a significant boost in the optical properties of the MoWOx formulations in comparison to the parent oxides. In a second step, the particles could be partially reoxidized during the remainder of the reaction time, due to their prolonged contact with the hydrogen peroxide (H_2O_2) reagent present in the synthetic media; this could result in the 1 h samples exhibiting a greater absorption signal than their 12 h counterparts.

In order to confirm the preliminary assumptions on free electron density made from these optical results, XPS analysis is performed to evaluate the composition and oxidation states at the surface of the different compounds (**Figure 4** and Table S1 (Supporting Information)). As for MoWOx samples, regarding molybdenum, both oxidized Mo^{6+} and reduced Mo^{5+} species are identified in MoWOx 1 and 12 h as doublet contributions on Mo3d signals, respectively, at 233.6/236.8 and 232.4/235.5 eV. For tungsten, only W^{6+} (and thus no W^{5+}) appears upon fitting of the W4f signals (doublet at 36.4/38.5 eV), highlighting the preferential trapping of the electrons over the molybdenum metallic centers at the surface of the particles.[14,43,57] The significant presence of reduced species is concomitant with the formation of oxygen defects in the crystal lattice, with some of the excess in electrons left from the missing oxygen trapped by metal atoms.[8,12,57,58] In addition, and even though this interpretation might be subject to much debate in the XPS field,[59] the presence of oxygen vacancies (O_{vac}) could be supposed from the O1s signal, with a contribution at 532.6 eV which also appears to be of the same intensity between both formulations. These results show very similar electronic surface properties in the mixed oxides, regardless of the time under solvothermal treatment. However, since XPS only probes the surface of the particles, the differences observed in the optical properties could arise from the bulk of the particles. As for the $WO_{3-\delta}$ parent oxide, a significant proportion of the W metallic centers are found to be in the W^{5+} state. Regarding O1s, the $WO_{3-\delta}$ 1 h exhibits similar amounts of O_{vac} to those found in the mixed oxide samples, while this contribution in the 12 h formulation is found to be significantly less intense. In addition, the signal at 533.5 eV corresponds to weakly adsorbed C—O and O—H organic species. The increased contribution of the latter in $WO_{3-\delta}$ 12 h (especially in view of the 532.1 eV signal) could indicate favorable crystalline faces at the surface of the hexagonal platelets, leading to a greater adsorption of organic impurities on the outer layer of the particles.

For semiconductor materials to support plasmonic features, such as the $WO_{3-\delta}$ materials investigated in this work, it
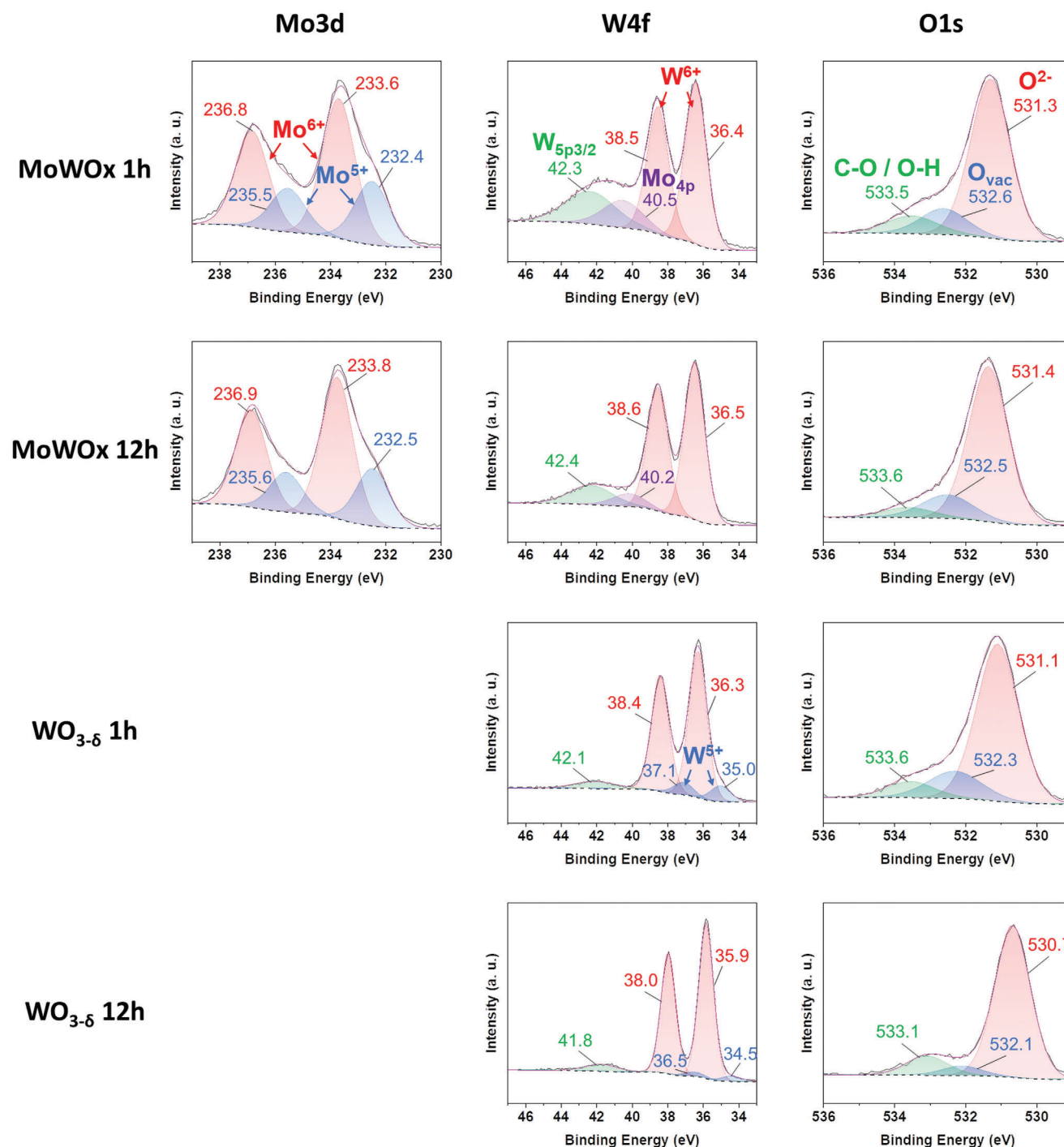
ADVANCED
SCIENCE NEWS

www.advancedsciencenews.com

ADVANCED
OPTICAL
MATERIALS

www.advopticalmat.de

Figure 4. Mo3d, W4f, and O1s XPS spectra of the MoWOx 1 h, MoWOx 12 h, WO$_{3-\delta}$ 1 h, and WO$_{3-\delta}$ 12 h powders.

is necessary that their concentration in free charge carriers increases beyond a threshold, after which the material undergoes a transition to a degenerated semiconductor displaying a metallic behavior.[60–62] The four investigated formulations all support a large amount of reduced species and O$_{vac}$, leading to an oxygen substoichiometry that allows these WO$_3$-based materials to present LSPR properties.[50] That said, the lower concentration in reduced species and O$_{vac}$ obtained for WO$_{3-\delta}$ 12 h in compar-

ison with the other formulations, as well as the large dimensions of the hexagonal particles (≈2 µm), could limit their use as efficient plasmonic electrochromic materials.

Finally, Mo/W ratios are calculated, showing again that molybdenum-rich compositions are obtained for short-duration syntheses, with 3.7 and 1.6 Mo/W ratios determined for 1 and 12 h, respectively, starting from a 2/1 ratio of Mo/W precursors in the reactive media. These results confirm that faster reaction
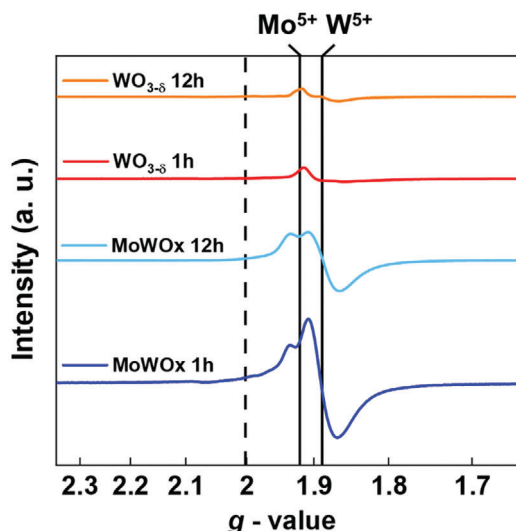
2401995 (6 of 16)

ADVANCED
SCIENCE NEWS

www.advancedsciencenews.com

ADVANCED
OPTICAL
MATERIALS

www.advopticalmat.de

Figure 5. Low temperature X-band EPR spectra of the MoWOx 1 h, MoWOx 12 h, WO$_{3-\delta}$ 1 h, and WO$_{3-\delta}$ 12 h powders.

kinetics occur for the Mo species, leading to a gradient going from the center of the urchins to the outer layer of surface nanorods. Noteworthy, Mo/W ratios calculated from XPS are smaller than EDX ones (see Figure S2 in the Supporting Information), being of 4.7 and 2.0 for 1 and 12 h by EDX, respectively. Since the XPS only probes the surface of the material, in comparison to the depth of analysis in the EDX measurements giving access to the bulk of the particles, XPS ratios are logically smaller than EDX ones, further pleading for a concentric distribution of the Mo within the mixed oxide particles.

Electron paramagnetic resonance (EPR) characterization is then carried out to assess the presence of free electrons, not only at the surface, as it is the case with XPS, but also in the bulk of the materials. This method allows the detection of unpaired electrons, such as those trapped in oxygen vacancies, those localized over reduced species such as W^{5+} (5d^1, $g \leq 1.9$) and Mo^{5+} (4d^1, $g \geq 1.9$) or those delocalized into the conduction band ($g < 2$). All four samples show large and well-defined signals below g-values of 2 (**Figure 5**), indicating that the electrons liberated by the formation of oxygen vacancies during the synthesis are either preferentially localized over metallic ions (yielding Mo^{5+} and W^{5+} reduced species), or delocalized into the conduction band to participate in the free charge carrier concentration. If the electrons were to be trapped inside the vacancies, the measured EPR response would rather appear as a very narrow signal, centered around a g-value close to 2.0023, corresponding to the free electron in vacuum (see the dashed line in Figure 5). The absolute concentration in all paramagnetic species, regardless of the proportion in the different elements (either reduced Mo or W, or free electrons in the conduction band), is proportional to the number of spins in the samples and to the area under the EPR absorption curves (Figure S8 and Table S2, Supporting Information), calculated by integration. Thus, the double integration of the EPR spectra follows a trend regarding the concentration in reduced species and free electrons in the conduction band: MoWOx 1 h > MoWOx 12 h > WO$_{3-\delta}$ 1 h > WO$_{3-\delta}$ 12 h (cf. Figure S8 in the Supporting Information), in good agreement with the ranking of optical

absorption intensity (see Figure 3). In the bulk, MoWOx 12 h has therefore 45% less reduced species and free conducting electrons than its 1 h counterpart, while the signal of WO$_{3-\delta}$ 1 and 12 h only represents 11% and 7% of that measured in the MoWOx 1 h case.

All in all, there is a globally good match between XPS and EPR electronic measurements, and also with the UV–VIS–NIR optical results presented above. Consequently, the presence of a higher quantity in free charge carriers, delocalized in the conduction band or localized on reduced species, whether at the surface or in the bulk of the materials, seems to translate into an increased absorption of the particles.

2.2. Spin-Coated "MoWO$_x$" and WO$_{3-\delta}$ Films

2.2.1. Morphology and Topography

MoWOx and WO$_{3-\delta}$ films are then deposited on glass substrates by spin coating (see details in the Experimental Section), and SEM top view microscopy images of the samples are presented in Figure S9 (Supporting Information). Using a similar deposition protocol in all four cases, with equivalent quantities of each material being deposited at the surface of the substrate (same concentration and deposited volume across all suspensions), quite homogeneous films are obtained with thicknesses of 1.16 ± 0.05 µm for MoWOx 12 h, 0.21 ± 0.02 µm for WO$_{3-\delta}$ 12 h, 0.84 ± 0.03 µm for MoWOx 1 h, and 0.87 ± 0.03 µm for WO$_{3-\delta}$ 1 h (Figure S10, Supporting Information). The strong decrease in thickness observed for the WO$_{3-\delta}$-12 h-based films probably arises from a preferential organization of the hexagonal WO$_{3-\delta}$ particles as lying parallel to the surface of the substrate, and from a less homogeneous deposition process leading to noncovered regions of the substrate, (being observable in the microscopy image, Figure S9D). In the case of the WO$_{3-\delta}$ 1 h formulation (Figure S9C), the nanoparticles observed in the parent oxide rearrange themselves as microscale aggregates, leading to the deposition of a film with similar morphology and thickness to that of the 1 h mixed oxide (Figure S9A). Besides, films of MoWOx 12 h (Figure S9B) are thicker in comparison with the other formulations, given the larger radius of the urchins obtained for this synthetic protocol.

2.2.2. Ex Situ Electrochemistry

The active layers are then characterized by cyclic voltammetry (CV) in a 0.5 M lithium perchlorate (LiClO$_4$) in propylene carbonate (LiClO$_4$/PC) electrolyte solution. A characteristic curve is obtained for both WO$_{3-\delta}$ formulations (**Figure 6**), with a reduction wave starting around -0.1 V (vs Ag/AgCl) and a return oxidation peak around -0.8 V. In the case of the MoWOx films, the general shape of the CV is retained while the anodic peak appears to comprise two overlapping signals, that could correspond to the oxidation of tungsten (into W^{6+}) around -0.8 V, and molybdenum (into Mo^{6+}) at -0.3 V. The capacity extracted from these electrochemical measurements, presented in **Table 1**, highlights at least a threefold increase in capacity in the MoWOx layers in comparison with the WO$_{3-\delta}$ ones, notably the two 1 h samples being of similar thicknesses of 0.8–0.9 µm: 42.8 mC cm^{-2} for MoWOx, 13.5 mC cm^{-2} for WO$_{3-\delta}$. This large improvement in
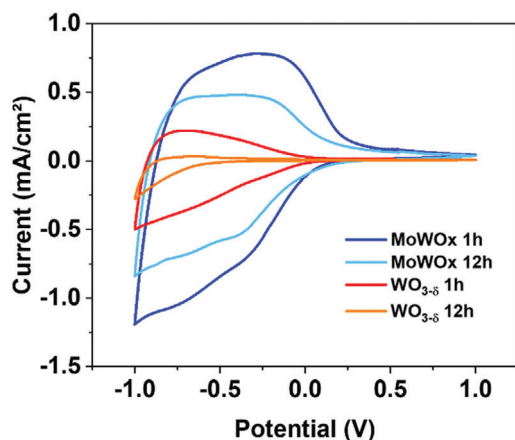
**ADVANCED
SCIENCE NEWS**

www.advancedsciencenews.com

**ADVANCED
OPTICAL
MATERIALS**

www.advopticalmat.de

Figure 6. CV curves (5th cycle at 20 mV s^{-1}, measured in 0.5 M LiClO$_4$/PC vs Ag–AgCl) of MoWOx 1 h (blue), MoWOx 12 h (cyan), WO$_{3-\delta}$ 1 h (red), and WO$_{3-\delta}$ 12 h films (orange).

capacity probably arises from the presence in large amounts of molybdenum in the mixed formulations,[45] for which theoretical capacity (MoO$_3$, 1117 mAhg^{-1}[63]) is superior to that of WO$_3$ (693 mAhg^{-1}[64]). Indeed, Elezzabi and co-workers have reported that while W can mostly be reduced from W^{6+} to W^{5+}, Mo can be reduced from Mo^{6+} to Mo^{5+} and then further reduced to Mo^{4+} if the structural properties of the material allow it, resulting in the exchange of an additional electron and thus a higher specific capacity.[45] In addition to the redox properties of both oxides, the crystalline structure adopted by the material also comes into play, allowing more or less cationic insertion into the crystal lattice. Even though the presence of Mo^{4+} in our mixed oxides has not been highlighted in this work, notably in view of the XPS results, it is expected that the capacity of the mixed oxides would increase in comparison to the pure tungsten parent oxides, given that our MoWOx formulations consist mostly in molybdenum. Following a similar argument, the capacity of MoWOx 1 h is greater than that of MoWOx 12 h, 42.8 versus 28.9 mC cm^{-2}, as expected from the Mo-rich 1 h compound (5/1 Mo/W ratio vs 2/1 for the 12 h sample, as established from EDX analyses). Even though the thickness of both films differs, a globally similar concentration of material per unit area is expected due to the smaller particles of MoWOx 1 h being more closely packed at the surface of the substrate. On the other hand, the large urchins obtained after 12 h result in more free space in the film due to lower compaction of the material, resulting in a well thicker but less dense layer. Therefore, considering comparable materials quantities in both films, the enhanced capacity of MoWOx 1 h versus MoWOx 12 h

is expected to arise from a greater Mo content per unit area in this sample. The presence of a large concentration in oxygen vacancies (responsible for the release of numerous unpaired electrons, leading to the intense EPR response of the mixed oxides) could also be the reason for the observed increase in capacity, possibly enhancing the conductivity of the sample and acting as active sites for the redox reactions.[65,66]

2.2.3. In Situ Spectro-Electrochemistry

Contrasts and Coloration Efficiencies: Spectro-electrochemical (SEC) characterization of the films is carried out in potentiostatic mode to study their dual-bald electrochromic functionality. Similarly to the electrochemical measurements above, 0.5 M LiClO$_4$ in propylene carbonate is used as electrolyte. Here, various potential values, progressively decreasing from +1.0 to −1.0 V versus Ag–AgCl by 0.5 V steps, are applied for 5 min each before the acquisition of the transmittance spectra between 350 and 1650 nm, and this in order to reach a stable optical state. The quantified transmittance values are expressed as the averaged transmittance over a given range of wavelength (350–750 nm for the VIS region, and 750–1650 nm for the NIR range, see the Experimental Section). The 100% of transmittance reference is acquired measuring the electrochemical cell containing the electrolyte and an uncoated FTO-glass substrate as "blank" sample, in order to only analyze the impact of the active (coated) material in the SEC measurements. As shown in **Figure 7** and **Table 2**, both MoWOx formulations and WO$_{3-\delta}$ 1 h display a dual-band behavior, as described above, evolving from a bleached state at +1.0 V, to an intermediate state displaying LSPR-based NIR darkening abilities at progressively reduced potentials (+0.5 and +0.0 V). Then, as the voltage reaches more reducing values, the transmittance keeps lowering in the NIR and starts to decrease in the VIS region as well, allowing a third, fully darkened optical state. Interestingly, no dual-band behavior is observed in the WO$_{3-\delta}$ 12 h, certainly as the consequence of its (deduced) low quantity in free charge carriers, reduced species, and oxygen vacancies (as shown from the combination of EPR and XPS results), as well as the micrometric dimension of the particles limiting their ability to support LSPR features.

According to previous electrochromic literature,[1,2,4,17,30] the behavior of dual-band materials, requiring different potential ranges to activate the desired modulation, relies on competitive polaronic versus plasmonic mechanisms, which are based on Faradaic versus capacitive charge/discharge processes. The considered studies suggest first a plasmonic-based NIR-selective modulation that should be active at slightly reducing potentials, given its capacitive behavior, with the Faradaic process then occurring once more reducing potentials are reached – which is required to promote the insertion of cations from the electrolyte into the active material.[1,2,4] Even though this approach is considered for the discussion of the results presented later in this work, other interpretations have been proposed (see Introduction), especially questioning the link between the capacitive/Faradaic mechanisms and the plasmonic/polaronic activity they are, respectively, associated with.[4,17–20,22–24] In this case, the first model seems plausible for the presently studied systems.

Table 1. Capacity calculated from the CV curves of MoWO$_x$ 1 h, MoWO$_x$ 12 h, WO$_{3-\delta}$ 1 h, and WO$_{3-\delta}$ 12 h films.

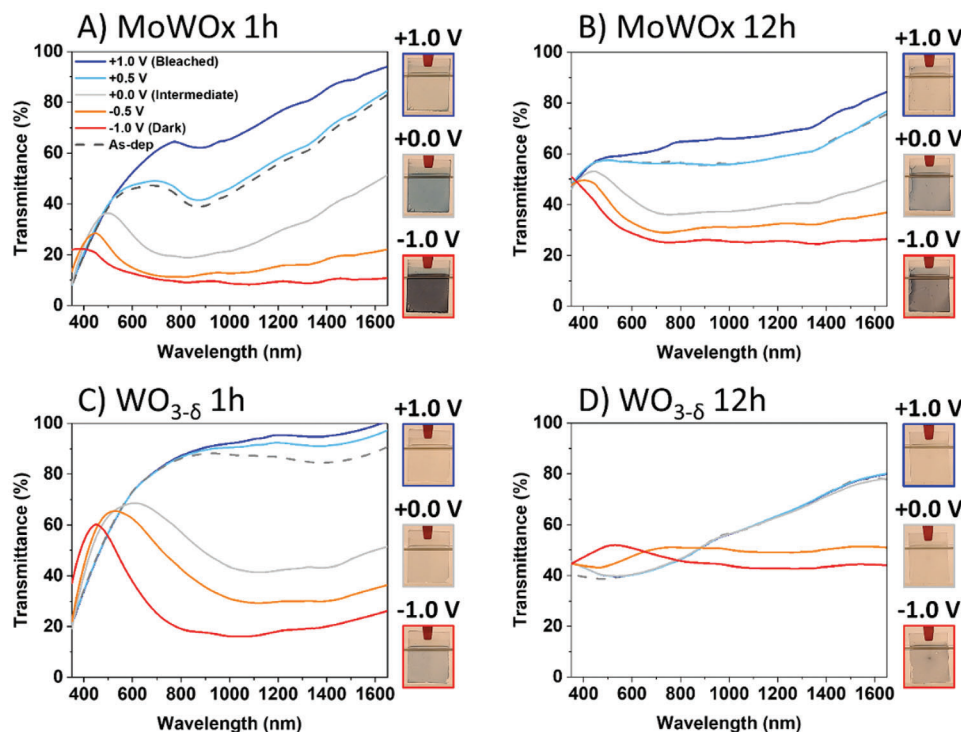|		Capacity [mC cm^{-2}]	Identified oxidation peaks
MoWOx	1 h	42.8	−0.7, −0.4 V
MoWOx	12 h	28.9	−0.7, −0.4 V
WO$_{3-\delta}$	1 h	13.5	−0.7 V
WO$_{3-\delta}$	12 h	3.3	−0.6 V

Figure 7. SEC transmittance spectra of A) MoWOx 1 h, B) MoWOx 12 h, C) $WO_{3-\delta}$ 1 h, and D) $WO_{3-\delta}$ 12 h films biased in the $LiClO_4$–PC electrolyte, as a function of the applied potential. Pictures of the films in the bleached (+1.0 V), intermediate (+0.0 V), and dark states (−1.0 V) are shown as insets next to the corresponding spectra.

Photographs illustrating the appearance of the films produced from all four formulations as a function of the applied potential are further presented as insets in Figure 7, and their $L^*a^*b^*$ parameters are included in Table S3 (Supporting Information). Very interestingly, the electrochromic properties exhibited by the MoWOx formulations, especially the 1 h case, appear to deviate from the usual dual-band behavior, as reported in the literature for $WO_{3-\delta}$-based materials[4,14–17] and recalled in the previous paragraph. Indeed, in their most oxidized state (at +1.0 V), MoWOx 1 and 12 h display some absorption in the VIS range (46.8% and 58.1% of respective averaged transmittance) together with relatively high transparency in the NIR (averaged transmittance of 76.1% and 70.5%, respectively). This optical absorption response arises from the strong, enhanced absorption signal provoked by the Mo–W mixing (see Figure 3), that in turn lowers the maximal transmittance values that can

be reached in the wavelength range around its maximum optical response (here 850–900 nm, corresponding to the superposition of the polaronic and plasmonic signals observed in the optical characterization of the powders). Instead of going from a VIS-bright state to first an intermediate cool state (VIS-bleached, NIR-darkened) and then a fully VIS- and NIR-darkened state, the MoWOx samples start from a "warm" transmission state (NIR-transparent and VIS-darkened), then undergo NIR opacification before finally achieving the fully VIS- and NIR-darkened state. The interest for such warm state,[29–31] with consecutive NIR then VIS modulation, is well established in the electrochromic literature, while being reported as posing challenges by being difficult to obtain from single-component dual-band material;[67] in fact, it is rather attained by designing cathode@anode electrochromic composites (such as $WO_{3-\delta}$@PB[68] and ITO NCs@PANI[31]), by utilizing the coloring of counter electrode (such as WO_{3-x}

Table 2. Summary of the SEC data in $LiClO_4$–PC.

	Bleached (+1.0 V)		Intermediate (+0.0 V)							Dark (−1.0 V)						
	T [%]		T [%]		ΔT [%]		Q_{in} [mC cm^{-2}]	CE [cm^2 C^{-1}]		T [%]		ΔT [%]		Q_{in} [mC cm^{-2}]	CE [cm^2 C^{-1}]
	VIS	NIR	VIS	NIR	VIS	NIR		VIS	NIR	VIS	NIR	VIS	NIR		VIS	NIR
MoWOx 1 h	46.8	76.1	31.1	30.8	15.8	45.3	−11.2	15.9	35.1	23.3	9.5	23.5	66.6	−82.1	3.7	11.0
MoWOx 12 h	58.1	70.5	45.0	40.5	13.0	30.0	−9.6	11.5	25.1	34.0	25.5	24.0	45.0	−59.0	3.9	7.5
$WO_{3-\delta}$ 1 h	61.3	93.8	58.7	46.3	2.6	47.5	−3.0	6.3	102.2	42.6	19.4	18.7	74.5	−32.7	4.8	21.0

**ADVANCED
SCIENCE NEWS**

www.advancedsciencenews.com

**ADVANCED
OPTICAL
MATERIALS**

www.advopticalmat.de

combined with V-doped TiO$_2$[29]), or by optimizing the electrolyte and/or integrating other technological components, such as thermochromic ones.[67] Regarding single-component formulations, some studies conducted notably on V-doped[29] or Nb-doped TiO$_2$[30,69] have already shown interesting related properties, acknowledging the occurrence and performance of a VIS-darkened, NIR-transmissive warm state; nevertheless, it has not been reported yet for Mo- or W-based electrochromic formulations, to the best of our knowledge.

Therefore, one hypothesis to explain the peculiar behavior expressed in the MoWOx formulation lies in the large number of reduced species created during the solvothermal synthesis: if the concentration in reduced species is too high, the density of polaronic states is so large that the application of an external bias is not sufficient to completely oxidize the material back to the bright state, explaining the residual light blue coloration of the film (see inset in Figure 7A). In addition, the large size of the particles leads to an increased thickness of the films, as well as a large contribution of the diffuse transmittance, resulting in the loss of some proportion of transmittance in the visible range. Meanwhile, the plasmonic contribution can be modulated over a wide range of transmittance levels, as the plasma frequency can be tuned by the application of an oxidizing potential to allow a high transmittance in the NIR, redshifting the plasmonic signature into higher wavelengths. With both effects combined, considering the most oxidized state, the MoWOx ends up in an optical state where the plasmon lies too far into the NIR to influence the transmittance of the film, while the residual polaronic activity and scattering of the urchin-like particles both limit the transparency of the active layer in the visible range. In comparison, MoWOx 12 h exhibits a weaker optical activity, but is still subject to an important diffuse transmittance from the large particles at the surface of the substrate. On the other hand, WO$_{3-\delta}$ 1 h presents a less intense optical signature than MoWOx 1 h, and is made of smaller particles less prone to light diffusion. This results in a higher VIS transmittance in the 1 h parent oxide, followed by MoWOx 12 h and finally MoWOx 1 h. The WO$_{3-\delta}$ 12 h film appears as less transparent than the other formulations, in fact switching between an opaque white state and an opaque blue state. In addition, this material does not exhibit the sought for dual-band electrochromic behavior, therefore, the latter cannot be considered as an interesting candidate for the independent modulation of VIS/NIR wavelengths.

In the case of MoWOx 1 h, contrasts of 15.8% and 45.3% are obtained for the intermediate state, in the VIS and NIR regions, respectively, while the colored state exhibits a modulation of 23.5% and 66.6% in those same ranges. The coloration efficiency of the active materials (CE, in cm^2 C^{-1}) corresponds to the density of optical modulation per unit of inserted charges (see the Experimental Section for the formula). The CE of the material reaches values of 15.9 cm^2 C^{-1} (VIS) and 35.1 cm^2 C^{-1} (NIR) in the intermediate state, and 3.7 cm^2 C^{-1} and 11.0 cm^2 C^{-1} in the darkened state. The MoWOx 12 h displays a modulation of 13.0% in the VIS and 30.0% in the NIR at +0.0 V, then these values, respectively, go up to 24.0% and 45.0% once −1.0 V is applied. This formulation displays CE of 11.5 and 25.1 cm^2 C^{-1} in the NIR-preferential state, and 3.9 and 7.5 cm^2 C^{-1} in the most reduced state, for VIS and NIR regions, respectively. For the third dual-band formulation, WO$_{3-\delta}$ 1 h, contrasts in the VIS and NIR ranges, respectively, reach 2.6% and 47.5% in the intermediate state, and 18.7% and 74.5% in the darkened state. In the latter case, the material exhibits CE values of 6.3 and 102.2 cm^2 C^{-1} at +0.0 V and 4.8 and 21.0 cm^2 C^{-1} at −1.0 V. For all three active formulations, the additional ability to further oxidize the "as-deposited" state by applying a +1.0 V potential is in good agreement with the assumption that the formation of reduced species, especially with MoWOx configurations, could be due (at least partially) to the insertion of protons provided by the isopropanol in the reactive media into the crystal lattice during the solvothermal process,[8] which can in turn be extracted from the material during the electrochemical cycling. The fourth case, WO$_{3-\delta}$ 12 h, has not been evaluated in terms of figures of merit in view of its poor intrinsic EC behavior.

Noticeably, in the three considered formulations, the CE of the intermediate state is clearly superior to that of the darkened state: indeed, almost half of the total optical change (especially in the NIR) is already reached at +0.0 V for only 10–16% of the total charge inserted in the darkened state. As stated earlier, such high efficiency can be linked to a capacitive behavior. These results, in addition to the optical and electronic characterizations of the precursor powders presented earlier, attest the ability of the two MoWO$_x$ formulations, as well as the WO$_{3-\delta}$ 1 h, to support a dual-band behavior being potentially LSPR-based. From the contrast and CE values presented in Table 2, MoWO$_x$ 1 h shows better performances than its 12 h counterpart, especially in the NIR region. This improved behavior for shorter solvothermal treatment could result from the differences observed in the powders, with smaller particle size and increased free charge carrier concentration (as shown in the EPR spectra, Figure 5), leading to a higher surface area and an enhanced optical absorption (see Figure 3).

Kinetics: In addition to its contrasts and CEs, the performance of an electrochromic material also depends on its ability to switch between optical states in an adequate time frame. Presently, the kinetics of the films are measured at three wavelengths: 550, 1000, and 1550 nm, during 10 min for each potential step. The so-called coloration/bleaching times (t_c and t_b, respectively) correspond to the duration required to reach 90% of the contrast between the bleached and colored state (or reversibly). The coloration and bleaching kinetics of the two MoWOx and the WO$_{3-\delta}$ 1 h samples are summarized in **Figure 8** and **Table 3**.

To begin with, for all three formulations, the coloration time in the VIS region at the intermediate bias (+0.0 V) appears very long for a very limited modulation (around 10% at best), reaching values ranging from 300 to 500 s. Besides, the NIR modulation takes place at faster rates, with a maximum in t_c of 198 s, while displaying greater contrasts (close to 40%). These results highlight the NIR-selective modulation (mainly plasmonic) exhibiting faster kinetics than the VIS modulation (mainly polaronic). During the reverse bleaching step, the discoloration in both VIS and NIR regions is carried out at significantly faster paces, with the exception of MoWOx 1 h in the NIR range, exhibiting the longest bleaching times recorded across the three investigated formulations. Regarding the dark state (−1.0 V), the coloration appears very quick since the greater difference in potential allows the easier insertion of the Li$^+$ cations from the electrolyte into the active layer, resulting in fast kinetics even for large contrasts (30−40% and 60−80% in the VIS and NIR regions, respectively). The
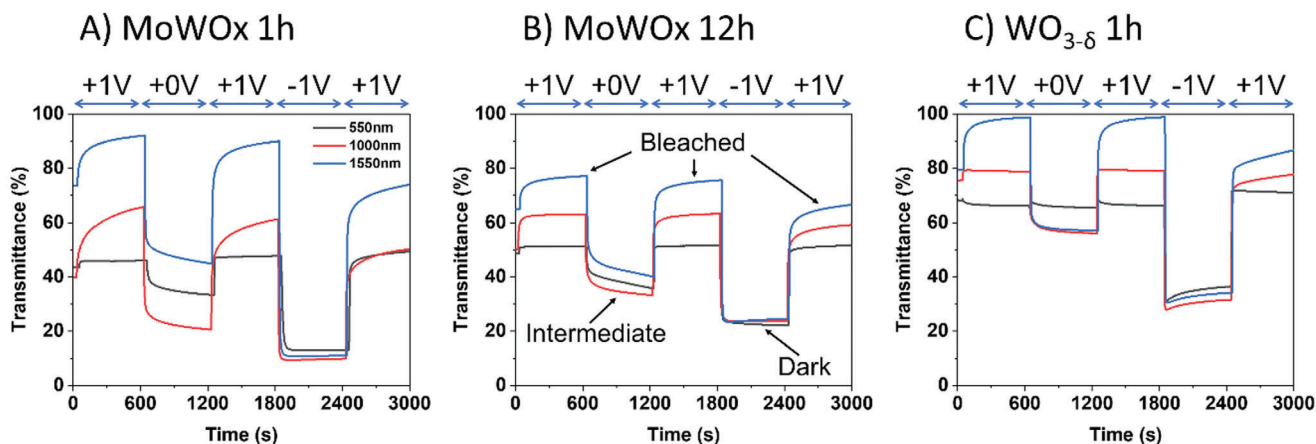
**ADVANCED
SCIENCE NEWS**

www.advancedsciencenews.com

**ADVANCED
OPTICAL
MATERIALS**

www.advopticalmat.de

Figure 8. SEC transmittance curves of the films obtained from the three dual-band formulations A) MoWOx 1 h, B) MoWOx 12 h, C) WO$_{3-\delta}$ 1 h, as a function of time and applied potential, for three distinct wavelengths (black curve: 550 nm, red curve: 1000 nm, blue curve: 1550 nm).

discoloration of the darkened state is faster in the VIS region, while the bleaching in the NIR presents slower kinetics, probably due to charge trapping inside the particles, leading to residual darkening after the electrochemical cycling.

Globally, these results highlight the ascendancy of the capacitive mechanisms at moderate bias, which is then caught up by the Faradic behavior once a more reducing potential is applied. However, in comparison with other plasmonic materials of the literature,[4,17] quite long switching times are noticed for the NIR modulation, especially for both MoWOx 1 and 12 h in comparison to WO$_{3-\delta}$ 1 h. On the basis of the results presented here, these slow kinetics could be due to the complexity of the urchin-like MoWOx particles that somehow hinders the available surface area and increases the mean free path of the positive counterions (here, Li$^+$ cations) that have diffused from the bulk electrolyte to the active material surface. In the case of MoWOx 1 h, the smaller dimensions of the particles translate into an even more compact packing of the nanorods around the core, further impeding the diffusion of the cations toward the active surface. In comparison, the nanospherical morphology of the WO$_{3-\delta}$ 1 h offers larger surface area and shorter diffusion paths, thus globally improving the commutation kinetics for this material.

Capacitive versus Faradic Mechanisms: In order to further analyze the capacitive behaviors expected from the materials, the spin-coated films are electrochemically biased in potentiostatic mode in a 0.5 м tetrabutylammonium perchlorate (TBAClO$_4$)–PC electrolyte, with capacitive values directly extracted from the EClab software analysis. Given the very large radius of the TBA$^+$

cations, ionic insertion into the crystal lattice of the active layers is prohibited. Therefore, any measured optical change has to originate from a capacitive charge/discharge of the materials. This limitation in the available electrochemical processes is clearly visible in the transmittance spectra and data presented in Figure S11 and Table S4 (Supporting Information), with the darkening taking place preferentially in the NIR and reaching optical states similar to the +0.0 V intermediate state obtained with the lithiated electrolyte. Indeed, the MoWOx 1 h reaches contrasts of 10.4% (VIS) and 32.9% (NIR) in the intermediate state (+0.0 V), going up to 12.3% (VIS) and 44.3% (NIR) when applying −1.0 V. In the 12 h mixed oxide, the VIS contrast ranges from 8.0% at +0.0 V and 8.1% at −1.0 V, while the NIR modulation in the intermediate state comes up to 23.6% and 24.4% in the colored state. Besides, the 1 h parent oxide displays contrasts of 0.5% (VIS) and 22.2% (NIR) in the intermediate +0.0 V state, and −0.4% (VIS) and 26.3% (NIR) in the darkened state. Finally, in the case of WO$_{3-\delta}$ 12 h, no modulation appears upon cycling in TBAClO$_4$, indicating the lack of sufficient optoelectronic features in order to display the sought dual-band behavior. Pictures of the films are included as insets in Figure S11 (Supporting Information) while the L*a*b* parameters of the films are summarized in Table S5 (Supporting Information). In all three dual-band active formulations, the modulation in TBAClO$_4$ almost reaches completion at +0.0 V, with a few extra percent of contrast gained when a bias of −1.0 V is achieved, recreating an optical state very similar to the intermediate state (+0.0 V) that was obtained in the lithiated electrolyte. These performances are in good accordance with

Table 3. Summary of the SEC kinetics data obtained on MoWOx 1 h, MoWOx 12 h, and WO$_{3-\delta}$ 1 h films.

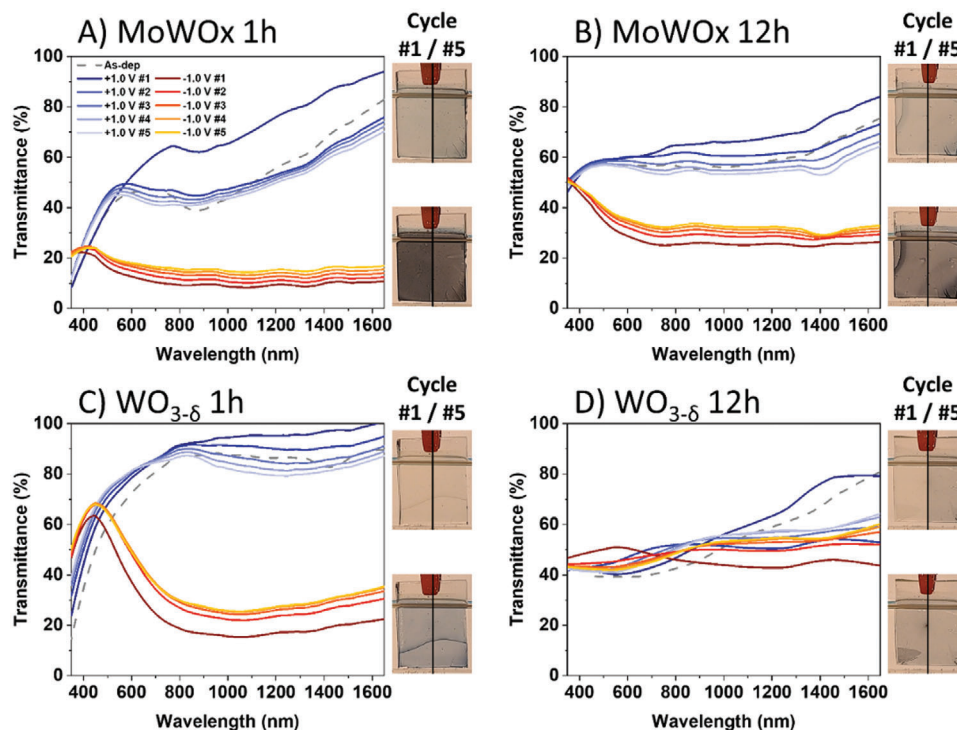|	Intermediate (+0.0 V)						Dark (−1.0 V)					
	t_c [s]			t_b [s]			t_c [s]			t_b [s]		
	550 nm	1000 nm	1550 nm	550 nm	1000 nm	1550 nm	550 nm	1000 nm	1550 nm	550 nm	1000 nm	1550 nm
MoWOx 1 h	304	74	110	6	252	140	28	8	10	58	160	114
MoWOx 12 h	410	138	198	6	52	80	16	16	10	14	106	104
WO$_{3-\delta}$ 1 h	484	88	22	2	4	72	6	4	6	4	24	68

Figure 9. SEC transmittance spectra of A) MoWOx 1 h, B) MoWOx 12 h, C) $WO_{3-\delta}$ 1 h, and D) $WO_{3-\delta}$ 12 h films biased in the $LiClO_4$–PC electrolyte, as a function of the electrochemical cycling.

what was expected from this experiment, limiting the modulation to the capacitive mechanisms, predominantly present in the intermediate state according to the model used for the interpretation of this work.

From the results, respectively, obtained in $LiClO_4$ and $TBAClO_4$, it is possible to estimate the proportion of capacitive-related modulation in the materials (cf. the Experimental Section for calculation details and Table S6 in the Supporting Information). These estimations show a greater percentage of the latter in the MoWOx formulations in comparison to the $WO_{3-\delta}$ 1 h: the capacitive mechanisms represent 69.2% and 70.1% of the intermediate state, and 59.4% and 44.0% of the darkened state of the MoWOx 1 and 12 h, respectively, while the 1 h parent oxide only exhibits 32.9% at +0.0 V and 18.7% at −1.0 V. These values are in good accordance with the optical and EPR characterizations of the powders presented above, which indicated a larger quantity of unpaired electrons in the MoWOx formulations in comparison to the pure oxides, with a significant proportion being delocalized in the conduction band and leading to a greater contribution of the capacitive behavior in the electrochromic performances of the materials. In addition, the decrease in capacitive contribution at −1.0 V, observed in all formulations, was anticipated since the electrochemical mechanisms in this second working regime are a combination of capacitive behavior and Faradaic charge/discharge in the lithiated electrolyte (while the $TBAClO_4$–PC electrolyte is limited to capacitive mechanisms). The same calculation can then be carried out for the inserted charges: since both the optical change and the quantity of inserted charges are important for the electrochromic performances of a material, the capacitive proportion of optical modulation can be divided by that of inserted charges in order to obtain a figure of merit equivalent

to the CE, but for the contribution of the capacitive behavior (K) in the different formulations (cf. the Experimental Section). Higher K values are consecutively determined for the mixed oxides in comparison to the parent oxide, with MoWOx 1 h displaying the greatest capacitive contribution out of the three dual-band formulations (1.46 and 1.79 in intermediate and darkened states, respectively, vs 1.12 and 1.30 for MoWOx 12 h, and 0.82 and 0.45 for $WO_{3-\delta}$ 1 h), once again highlighting the potential of this material for future developments.

Reversibility: Finally, an evaluation of the reversibility of the optical changes undergone by the different materials is performed. Transmittance modulation spectra of MoWOx 1 and 12 h, and of $WO_{3-\delta}$ 1 and 12 h samples are presented in **Figure 9**, being biased between +1.0 and −1.0 V for 5 cycles, with pictures of the first and fifth cycles as insets. In addition, the evolution of the $L*a*b*$ parameters of the films during the electrochemical cycling are shown in Table S7 (Supporting Information). In MoWOx 1 h, a significant drop of transmittance in the bleached state already appears after the second cycle (minus 20% in the NIR, stable in VIS), followed by a stabilization of the transmittance values in both bleached (+1.0 V; 43.6% and 51.6% in VIS and NIR, respectively) and darkened states (−1.0 V; 15.5% in VIS and 27.5% in NIR). The loss of transmittance appearing after the first coloration seems to indicate some propensity to irreversible Li^+ insertion in some of the active sites. On the other hand, MoWOx 12 h and $WO_{3-\delta}$ 1 h display a similar stability of the colored state (maximum of 5–6% change in MoWOx 12 h and 10–11% in $WO_{3-\delta}$ 1 h, versus 4–6% in $MoWO_x$ 1 h) but a more gradual decay of the bleached state (minus 7.1% and 4.4% after the first coloration in $MoWO_x$ 12 h and $WO_{3-\delta}$ 1 h, respectively). Nevertheless, in all 3 cases, an optical state similar

to the "as-deposited" state is obtained within the first two cycles. One possible explanation of this process could be that the H$^+$ potentially present in the "as-deposited" samples (originating from the reducing effect/proton-donor effect of the isopropanol in the reactive medium) can be electrochemically extracted from the materials, with the transmittance of the film increasing to reach the +1.0 V state. However, after the first coloration, due to their size difference, Li$^+$ could be irreversibly inserted in the sites previously occupied by the protons, irremediably modifying the crystalline properties of the material, as previously reported for other metal oxides (such as Li$_{1.12}$(Ni$_{0.425}$Mn$_{0.425}$Co$_{0.15}$)$_{0.88}$O$_2$,[70] Li$_x$H$_{1-x}$NbO$_3$,[71] H$_2$Ti$_6$O$_{13}$,[72] MnO$_2$[73]) and thus limiting the transmittance of the films to their previous "as-deposited" state. Finally, in the case of the WO$_{3-\delta}$ 12 h, the bright and dark states almost completely merge after the first coloration cycle, thus not fulfilling the requirements to be considered as an electrochromic material, which should exhibit a reversible modulation of its optical properties upon the application of a potential.

All in all, the results obtained from the characterizations of the films highlight the remarkable properties of WO$_{3-\delta}$ 1 h and both MoWOx, especially MoWOx 1 h, as dual-band plasmonic electrochromic materials. In all active formulations, it was possible to demonstrate the preferential modulation of NIR wavelengths at slightly reducing potentials; the origin of this NIR-selective activity seems to arise from a capacitive/plasmonic behavior, as proposed from the SEC measurements in TBAClO$_4$–PC. Among the mixed oxides, MoWOx 1 h exhibits the most promising performances, owing to a greater quantity of free charge carriers leading to a greater optical absorption. Even though WO$_{3-\delta}$ 1 h displays faster kinetics and a more selective modulation toward NIR in the intermediate state (+0.0 V), a greater proportion in capacitive behavior is shown in both MoWOx formulations. In addition, the MoWOx formulations, especially the 1 h case, display a very peculiar and novel optical behavior in the as-deposited state and after +1.0 V polarization (bleached), involving a large transmittance in NIR coupled with relatively strong absorption in VIS corresponding to a warm optical state (VIS/light blocking and NIR/heat transparent). This novel optical state could result in a better adaptability of the devices in cold-weather regions and/or seasons, maximizing the transmitted heat while avoiding glares, thanks to the lowered VIS transmittance.

3. Conclusions

Novel electrochromic materials based on mixed molybdenum–tungsten oxide formulations (Mo$_y$W$_{1-y}$O$_{3-\delta}$, "MoWOx") have been obtained from a single-step solvothermal synthesis procedure. These compounds have been further spin-coated into thin films that attest for their dual-band optical modulation. Specifically, a VIS/NIR-selective electrochromic behavior is observed in MoWOx 2/1 formulations obtained after 1 and 12 h of synthetic duration; a preferential NIR darkening is obtained when a slightly reducing potential of +0.0 V (vs Ag/AgCl) is applied, followed by an opacification over both VIS and NIR regions when using a more reducing potential of −1.0 V. The dual-band properties exhibited by these materials are correlated to the presence of a large amount of unpaired electrons, obtained through the promoted formation of oxygen vacancies and reduced species during the synthesis, and to the presence of nanostructures (nanorods

at the surface of the MoWOx urchins) allowing them to support LSPR features. Among the mixed oxide formulations, MoWOx 1 h displays the most remarkable optical performances, with notably large transmittance contrasts in both VIS (23.5%) and NIR (66.6%) regions. Interestingly, MoWOx compounds testify for the occurrence of a warm state (VIS-darkened, NIR transparent) which, to the best of our knowledge, has not been reported so far with tungsten- or molybdenum-oxide-based electrochromic materials. This uncommon optical state is therefore uniquely obtained, thanks to the large quantity of free charge carriers originating from the Mo/W mixing process, leading to a strong optical absorption signal centered by 850–900 nm.

Within the scope of this research work, the dual-band electrochromism of MoWOx has been attributed to the presence of both plasmonic excitation (in NIR) and polaronic-like resonance (in VIS), in line with the proposed interpretation of the electrochemical response of reported WO$_{3-\delta}$ nanoparticles[1,2,4] and with the detailed analysis of the Kubelka–Munk experiment on the compounds studied herein.[48] The debate of the link between the doping mechanism (capacitive/Faradaic) and the type of excitation (plasmonic/polaronic) is however still open. Indeed, modeling works of the literature have shown that inserted cations are totally ionized and occupy existing cavities in WO$_3$ with no local deformation of the atomic structure.[19,74] In that case, both capacitive and Faradaic doping would have the exact same effect on the optical response. Nevertheless, further experimental and numerical investigations are required to settle the discussion, but this goes beyond the scope of the present work.

4. Perspectives

Future developments of MoWOx materials processing should be directed toward the consolidation of their electrochromic performances, notably their switching speed and reversibility. In addition, further research should be directed toward the full understanding, control, and optimization of the warm state, with a particular focus on further increasing the VIS transmittance of the MoWOx layers in their most oxidized state toward reaching a minimal 60% value (and ideally, 90+%), so to allow them to be more transparent upon user's request; this will certainly strengthen their applicability in optimally commutable applied dual-band electrochromic devices, progressively moving toward new smart windows being further industrialized then commercialized. If necessary, the synthetic and deposition processes could be adapted in order to obtain more favorable morphologies, optical and electronic properties, leading to improved performances of the films. Notably, developing MoWOx formulations with a narrower plasmonic contribution (e.g., by uniformizing the dimensions of the nanostructures and/or improving their crystallinity) could lead to an enhanced NIR selectivity in the intermediate state, as the plasmonic and polaronic contributions would present less overlap. As the plasma frequency of the MoWOx formulations lies right at the limit of the 800–1300 nm range of interest, a narrower plasmonic signal would result in an even higher and more efficient selectivity toward NIR radiations while maintaining an efficient modulation of the transmitted heat. In future works, additional numerical calculations, notably exploiting first principle approaches, should be considered to further describe and quantify the optical and electronic tuning

**ADVANCED
SCIENCE NEWS**

www.advancedsciencenews.com

**ADVANCED
OPTICAL
MATERIALS**

www.advopticalmat.de

occurring in MoWOx structures. In addition, several other synthetic paths could be explored, such as colloidal synthesis or supercritical processes, but also different deposition methods like spray coating,[75] allowing for the scale-up of the film processing. Finally, the next step after reaching convincing electrochromic properties will be to fabricate full devices. While long-term stability testing was not conducted in the scope of this work, this aspect is currently under investigation, looking into optimizing the counter electrode to be implemented in tandem with the MoWOx materials. Such strategy is anticipated to strengthen the durability and reversibility of the electrochromic processes.

With this work as a first demonstration of the original, advanced optical functionality of the MoWOx formulations, the results presented herein are very promising for the future development of highly efficient dual-band electrochromic systems based on these mixed oxide formulations. Relying on the enhanced efficiency and selectivity of these materials toward VIS and NIR wavelength ranges, and looking into their ability to access multiple working configurations, including the warm state, the MoWOx formulations are promising candidates for the development of "new generation" dual-band smart windows. Such a remarkable solar filtration behavior could ultimately be of great interest to improve the functionality of fenestration solutions in buildings by broadening the modes of solar tunability, and therefore the adaptability range of the devices toward different weathers, seasons, geographies, and/or user needs.

5. Experimental Section

Materials: W (fine powder, 99+%) and Mo (99+%) were purchased from Merck, isopropanol (technical) and H_2O_2 (33%) from VWR, LiF (99.8% anhydrous) was supplied from ROC/RIC, LiClO$_4$ (95% anhydrous) by Alfa Aesar, TBAClO$_4$ (99+%) and PC (99.7% anhydrous) from Sigma-Aldrich. 50 × 50 cm Planibel G fast (15 Ω sq^{-1}) glass panels were graciously supplied by AGC Glass Europe and manually cut into 2.0 × 2.5 × 0.4 cm conducting transparent substrates. All reagents were used as received without further purification.

Synthesis of $Mo_yW_{1-y}O_{3-\delta}$ and $WO_{3-\delta}$ compounds: In a typical solvothermal synthetic procedure,[8] H_2O_2 (11.5 mL) was added to tungsten metallic powder (3 mmol) and molybdenum metallic powder (6 mmol) (Mo/W molar ratio = 2/1) and magnetically stirred for 1 h, yielding a clear yellowish solution. This solution was mixed with isopropanol (69 mL) into a Teflon vessel (125 mL), which was then sealed in a stainless-steel autoclave, heated, and maintained at 160 °C for a duration varying from 1 to 12 h. Following the cooling of the solvothermal reactor down to room temperature, the obtained suspension was collected, centrifuged, and rinsed with ethanol 3 times, and finally dried under vacuum at 60 °C overnight. The protocol was repeated with adapted Mo/W ratio for the synthesis of the 1/1 (4.5 mmol of tungsten and molybdenum) and 1/2 formulations (6 mmol of tungsten and 3 mmol of molybdenum). For the $WO_{3-\delta}$ parent oxide, the same protocol was applied without the addition of molybdenum powder (thus, with 9 mmol of tungsten).

Film Deposition: Suspensions of each formulations were spin coated onto conducting glass substrates, previously cleaned by sonication in acetone and ethanol, further dried under compressed air stream, and finally treated by UV–O$_3$ for 20 min. A suspension in ethanol (50 μL, 125 mg mL^{-1}) was dynamically deposited onto the substrates, being rotated at 2000 rpm for 1 min. The samples were subsequently dried for 5 min at 100 °C on a hot plate, and further submitted to a "flash" heating treatment of 1 min at 250 °C on a hot plate.

Characterizations: Microscopy images of the particles were obtained from TEM using a TECNAI G^2 20 operated at 200 kV. Top-view images of the spin-coated films were acquired on a SEM TESCAN CLARA equipped

with an EDX detector, so to determine particles dimensions (excepted for the $WO_{3-\delta}$ 1 h, measured on the TEM images) and molar ratios of the mixed oxides. Film thickness was measured by a Dektak stylus profilometer. XRD patterns were acquired on a Bruker D8 DISCOVER with Cu Kα (λ = 1.5418 Å). Powder compositions were investigated using a Thermofisher K-alpha XPS, equipped with a monochromatic Al Kα source and calibrated with the adventitious carbon (C1s) peak being normalized at 285.0 eV. Bulk electronic properties were characterized by EPR with a Bruker ESP300E spectrometer operating at 9.54 GHz (X-band), with the spectra acquired at 4K using 20 mW microwave power and normalized in accordance to the mass of the sample, gain, and number of accumulated scans. UV–VIS–NIR data were recorded using a Shimadzu UV-3600i Plus spectrophotometer, with the absorption of the powders being measured using an integrating sphere (ISR-1503) and exploiting the Kubelka–Munk formalism (see below) to transform diffuse reflectance measurements into absorption-proportional data. SEC characterization of the films was carried out using the same spectrophotometer (without the integrating sphere), exploiting an adapted sample holder for a three-electrode configuration (consisting in the sample itself as working electrode, a Ag/AgCl reference electrode, and a Pt foil counter electrode) in an optical glass cell. The electrochemical bias was controlled with a Biologic SP-200 potentiostat/galvanostat. The spectra were graphically smoothed in OriginPro 2021 using the Savitzky–Golay method available in the software, fitting a polynomial of the second order over a moving window of 40 points.

Interpretation of the Optical Measurements: The powders were characterized in terms of optical absorption by measuring their diffuse reflectance through UV–VIS–NIR spectrophotometry, and applying the KM function.[8,13,47,76] Further details on the application of the KM formalism to various plasmonic materials, including MoWOx compounds, were given and discussed in a dedicated study.[48]

Briefly, the KM formalism (Equation (1)) correlated the diffuse reflectance of the sample R_∞ to the quotient of its absorption coefficient (k) and scattering coefficient (s)[48,77,78]

$$k/s = (1 - R_\infty)^2/2R_\infty \qquad (1)$$

Since both k and s were wavelength-dependent in plasmonic materials, k could not be deduced from a measurement of the pure powder. To resolve this issue, the sample was diluted in a white powder (LiF, in a LiF/sample ratio of 100/10) that possessed a constant diffusion coefficient and almost no absorption over the measurement interval. In these conditions, the diffusion coefficient of the mixture was constant at a value corresponding to that of the white powder, and the absorption coefficient only resulted from the studied material. The 10 wt% proportion in diluting agent was selected to best fulfill the KM conditions while keeping a good signal to noise ratio.[48] The absorption data were computed from the diffuse reflectance measurements using the KM formula, replacing the R_∞ term in the formula (Equation (1)) with the reflectance of the powder measured at a given wavelength.[75,76]

Interpretation of the Electrochromic Characterizations: In order to quantify the optical contrasts of the films in a more precise manner, the latter were computed taking in account the average transmittance over an interval of wavelength representing the VIS (350–750 nm) and NIR ranges (750–1650 nm), rather than extracted from the difference of transmittance values at a specific single wavelength characterization. The transmittance was integrated over the given intervals and then normalized in comparison to the reference signal, as described in Equation (2) below

$$T_{int.} = 100\frac{\int T(\lambda)\,d\lambda}{\int T_{ref.}(\lambda)\,d\lambda} \qquad (2)$$

where $T_{int.}$ is the integrated transmittance over the VIS or NIR interval, $T(\lambda)$ is the transmittance of the sample at any given λ wavelength, and $T_{ref.}(\lambda)$ is the transmittance of the reference, corresponding to 100% of transmittance at any given λ wavelength.

The average transmittance over a given interval was also used for the calculation of the CE (in cm^2 C^{-1}) of the electrochromically active layers, determined in both VIS and NIR ranges, from the transmittance spectra

and electrochemical data acquired during the SEC characterization, replacing the T_b, T_c (averaged values of transmittance in the bleached and colored states, respectively,) and Q_{in} (inserted charge cm^{-2}) terms accordingly in the following Equation (3)[40,79]

$$CE = (\log(T_b/T_c))/Q_{in} \tag{3}$$

Finally, as a way to quantify the capacitive behavior observed in the SEC characterizations in the TBAClO$_4$/propylene carbonate electrolyte, two figures of merits were defined: the first one was the proportion of capacitive behavior in the optical contrast ($\Delta T_{capa.}$, Equation (4)), averaged on the VIS and NIR ranges of the sample

$$\Delta T_{capa.} = 100\Delta T_{TBA+}/\Delta T_{Li+} \tag{4}$$

where ΔT_{TBA+} and ΔT_{Li+} are the optical contrasts measured in the TBAClO$_4$/propylene carbonate and LiClO$_4$/propylene carbonate electrolytes, respectively.

A second figure of merit was established to take in account the capacitive behavior in both optical and electrochemical data

$$K = \Delta T_{capa.}/\left(100Q_{in,TBA+}/Q_{in,Li+}\right) \tag{5}$$

In Equation (5), K is a unitless factor defined as the capacitive contribution and is calculated by dividing $\Delta T_{capa.}$ by the capacitive proportion of the inserted charge (in TBAClO$_4$/PC or LiClO$_4$/PC, respectively, $Q_{in,TBA+}$ and $Q_{in,Li+}$) in a given optical state (and thus at a given electrochemical bias).

Supporting Information

Supporting Information is available from the Wiley Online Library or from the author.

Acknowledgements

Conflict of Interest

The authors declare no conflict of interest.

Author Contributions

F.G. carried out the synthesis of the materials, their deposition into thin films, and the morphological, structural, optical, and electrochemical characterization of powder and film samples under direct supervision of J.D., P.C., R.C., and A.M., with additional guidance and suggestions provided by A.R. and L.H. G.S. took care of the acquisition of SEM and TEM images. M.L. and L.H. contributed to the optical characterization of powders using the Kubelka–Munk formalism. M.D. carried out RPE measurements. XPS characterizations were conducted by R.G. Film thickness was measured by B.F. using profilometry. All authors contributed to the discussion and interpretation of the data. F.G. wrote the first draft of the paper, M.L., L.H., and A.M. edited it, and all authors contributed to the writing of the final version.

Data Availability Statement

The data that support the findings of this study are available from the corresponding author upon reasonable request.

[1] A. Agrawal, S. H. Cho, O. Zandi, S. Ghosh, R. W. Johns, D. J. Milliron, *Chem. Rev.* **2018**, *118*, 3121.
[2] Y. Wang, E. L. Runnerstrom, D. J. Milliron, *Annu. Rev. Chem. Biomol. Eng.* **2016**, *7*, 283.
[3] S. A. Maier, *Plasmonics: Fundamentals and Applications*, Springer-Verlag, New York **2007**.
[4] E. L. Runnerstrom, A. Llordés, S. D. Lounis, D. J. Milliron, *Chem. Commun.* **2014**, *50*, 10555.
[5] L. Tegg, V. J. Keast, *Plasmonics* **2023**, *18*, 49.
[6] K. Adachi, T. Asahi, *J. Mater. Res.* **2012**, *27*, 965.
[7] T. Wang, Y. Xiong, R. Li, H. Cai, *New J. Chem.* **2016**, *40*, 7476.
[8] H. Yin, Y. Kuwahara, K. Mori, H. Cheng, M. Wen, Y. Huo, H. Yamashita, *J. Phys. Chem. C* **2017**, *121*, 23531.
[9] P. Li, L. Zhu, C. Ma, L. Zhang, L. Guo, Y. Liu, H. Ma, B. Zhao, *ACS Appl. Mater. Interfaces* **2020**, *12*, 19153.
[10] X. Zhong, Y. Sun, X. Chen, G. Zhuang, X. Li, J. G. Wang, *Adv. Funct. Mater.* **2016**, *26*, 5778.
[11] Y. Zhao, Q. Tang, B. He, P. Yang, *Int. J. Hydrogen Energy* **2017**, *42*, 14534.
[12] N. Zhang, A. Jalil, D. Wu, S. Chen, Y. Liu, C. Gao, W. Ye, Z. Qi, H. Ju, C. Wang, X. Wu, L. Song, J. Zhu, Y. Xiong, *J. Am. Chem. Soc.* **2018**, *140*, 9434.
[13] N. Xue, R. J. Yu, C. Z. Yuan, X. Xie, Y. F. Jiang, H. Y. Zhou, T. Y. Cheang, A. W. Xu, *RSC Adv.* **2017**, *7*, 2351.
[14] S. Zhang, S. Cao, T. Zhang, Q. Yao, A. Fisher, J. Y. Lee, *Mater. Horiz.* **2018**, *5*, 291.
[15] S. Zhang, S. Cao, T. Zhang, A. Fisher, J. Y. Lee, *Energy Environ. Sci.* **2018**, *11*, 2884.
[16] S. Zhang, Y. Li, T. Zhang, S. Cao, Q. Yao, H. Lin, H. Ye, A. Fisher, J. Y. Lee, *Appl. Mater. Interfaces* **2019**, *11*, 48062.
[17] B. Tandon, H.-C. Lu, D. J. Milliron, *J. Phys. Chem. C* **2022**, *126*, 9228.
[18] J. Kim, A. Agrawal, F. Krieg, A. Bergerud, D. J. Milliron, *Nano Lett.* **2016**, *16*, 3879.
[19] M. Okada, K. Ono, S. Yoshio, H. Fukuyama, K. Adachi, *J. Am. Ceram. Soc.* **2019**, *102*, 5386.
[20] W. Wang, A. Janotti, C. G. Van de Walle, *J. Mater. Chem. C* **2016**, *4*, 6641.
[21] S. K. Deb, *Sol. Energy Mater. Sol. Cells* **1995**, *39*, 191.
[22] S. Yoshio, K. Adachi, *Mater. Res. Express* **2018**, *6*, 026548.
[23] A. D. Walkingshaw, N. A. Spaldin, E. Artacho, *Phys. Rev. B* **2004**, *70*, 165110.
[24] H. Hassani, B. Partoens, E. Bousquet, P. Ghosez, *Phys. Rev. B* **2022**, *105*, 014107.
[25] B. Sajadi, M. Mirnaghi, M. Akhavan-Behabadi, N. Delgarm, A. Goudarzi, *Energy Equip. Syst.* **2021**, *9*, 1.
[26] S.-Z. Sheng, J.-L. Wang, B. Zhao, Z. He, X.-F. Feng, Q.-G. Shang, C. Chen, G. Pei, J. Zhou, J.-W. Liu, S.-H. Yu, *Nat. Commun.* **2023**, *14*, 3231.

[27] S. Zhao, B. Wang, N. Zhu, Y. Huang, F. Wang, R. Li, Y. Zhao, Q. Jiang, X. Wu, R. Zhang, *Carbon Neutralization* **2023**, *2*, 4.

[28] Y. Zhai, J. Li, S. Shen, Z. Zhu, S. Mao, X. Xiao, C. Zhu, J. Tang, X. Lu, J. Chen, *Adv. Funct. Mater.* **2022**, *1*, 2109848.

[29] M. Barawi, G. Veramonti, M. Epifani, R. Giannuzzi, T. Sibillano, C. Giannini, A. Rougier, M. Manca, *J. Mater. Chem. A* **2018**, *6*, 10201.

[30] C. J. Dahlman, Y. Tan, M. A. Marcus, D. J. Milliron, *J. Am. Chem. Soc.* **2015**, *137*, 9160.

[31] P. Yilmaz, M. Magni, S. Martinez, R. Maria Gonzalez Gil, M. Della Pirriera, M. Manca, *ACS Appl. Energy Mater.* **2020**, *3*, 3779.

[32] D. Zhou, F. Shi, D. Xie, D. H. Wang, X. H. Xia, X. L. Wang, C. D. Gu, J. P. Tu, *J. Colloid Interface Sci.* **2016**, *465*, 112.

[33] M. Lagier, A. Bertinotti, O. Bouvard, L. Burnier, A. Schüler, *Opt. Mater.* **2021**, *117*, 111091.

[34] M. A. Arvizu, G. A. Niklasson, C. G. Granqvist, *Chem. Mater.* **2017**, *29*, 2246.

[35] S. Xie, Z. Bi, Y. Chen, X. He, X. Guo, X. Gao, X. Li, *Appl. Surf. Sci.* **2018**, *459*, 774.

[36] J. M. O. R. De León, D. R. Acosta, U. Pal, L. Castañeda, *Electrochim. Acta* **2011**, *56*, 2599.

[37] B. Wang, W. Man, H. Yu, Y. Li, F. Zheng, *Materials* **2018**, *11*, 1627.

[38] A. Kumar, S. Chandra Prajapati, P. P. Sahay, *J. Sol-Gel Sci. Technol.* **2019**, *90*, 281.

[39] W. Li, J. Zhang, Y. Zheng, Y. Cui, *Sol. Energy Mater. Sol. Cells* **2022**, *235*, 111488.

[40] H. Li, J. Chen, M. Cui, G. Cai, A. L. S. Eh, P. S. Lee, H. Wang, Q. Zhang, Y. Li, *J. Mater. Chem. C* **2015**, *4*, 33.

[41] H. Li, J. Li, C. Hou, D. Ho, Q. Zhang, Y. Li, H. Wang, *Adv. Mater. Technol.* **2017**, *2*, 1700047.

[42] H. Li, L. Mcrae, A. Y. Elezzabi, *Appl. Mater. Interfaces* **2018**, *10*, 10520.

[43] L. Zhou, J. Zhu, M. Yu, X. Huang, Z. Li, Y. Wang, C. Yu, *J. Phys. Chem. C* **2010**, *114*, 20947.

[44] A. Arzola-Rubio, J. Camarillo-Cisneros, L. Fuentes-Cobas, V. Collins-Martínez, L. De la Torre-Sáenz, F. Paraguay-Delgado, *Superlattices Microstruct.* **2015**, *81*, 175.

[45] H. Li, L. McRae, C. J. Firby, M. Al-Hussein, A. Y. Elezzabi, *Nano Energy* **2018**, *47*, 130.

[46] Q. Wang, C. Li, W. Xu, X. Zhao, J. Zhu, H. Jiang, L. Kang, Z. Zhao, *Appl. Surf. Sci.* **2017**, *399*, 41.

[47] H. Yin, Y. Kuwahara, K. Mori, H. Yamashita, *J. Mater. Chem. A* **2018**, *6*, 10932.

[48] M. Lobet, F. Gillissen, N. Demoor, J. Dewalque, P. Colson, R. Cloots, A. Maho, L. Henrard, *ACS Appl. Opt. Mater.* **2025**, https://doi.org/10.1021/acsaom.4c00432, https://arxiv.org/abs/2406.02181.

[49] K. Machida, K. Adachi, *J. Phys. Chem. C* **2016**, *120*, 16919.

[50] X. Huang, M. A. El-Sayed, *J. Adv. Res.* **2010**, *1*, 13.

[51] K. B. Mogensen, K. Kneipp, *J. Phys. Chem. C* **2014**, *118*, 28075.

[52] C. A. Triana, C. G. Granqvist, G. A. Niklasson, *J. Appl. Phys.* **2015**, *118*, 024901.

[53] M. Sarr, N. Bahlawane, D. Arl, M. Dossot, E. Mcrae, D. Lenoble, *Appl. Surf. Sci.* **2016**, *379*, 523.

[54] W. K. Chow, C. M. So, C. P. Lau, F. Y. Kwong, *Org. Chem. Front.* **2014**, *1*, 464.

[55] J. E. Dominguez, L. Fu, X. Q. Pan, *J. Appl. Phys.* **2002**, *81*, 5168.

[56] N. M. Ahmed, F. A. Sabah, H. I. Abdulgafour, A. Alsadig, A. Sulieman, M. Alkhoaryef, *Results Phys.* **2019**, *13*, 102159.

[57] P. R. Patil, P. S. Patil, *Thin Solid Films* **2001**, *382*, 13.

[58] H. Yin, Y. Kuwahara, K. Mori, C. Louis, H. Yamashita, *Catal. Sci. Technol.* **2020**, *13*, 4141.

[59] H. Idriss, *Surf. Sci.* **2021**, *712*, 2.

[60] K. Manthiram, A. P. Alivisatos, *J. Am. Chem. Soc.* **2012**, *134*, 3995.

[61] E. L. Runnerstrom, Ph.D. Thesis, University of California, Berkeley **2016**.

[62] E. Salje, B. Güttler, *Philos. Mag. B* **1984**, *50*, 607.

[63] H. Zhou, X. Zou, K. Zhang, P. Sun, M. S. Islam, J. Gong, Y. Zhang, J. Yang, *Appl. Mater. Interfaces* **2017**, *9*, 18669.

[64] A. I. Inamdar, H. S. Chavan, A. Talha, A. Ahmed, S. Cho, J. Kim, Y. Jo, S. M. Pawar, Y. Park, H. Kim, H. Im, *Mater. Lett.* **2018**, *215*, 233.

[65] X. Lu, Y. Zeng, M. Yu, T. Zhai, C. Liang, S. Xie, M. S. Balogun, Y. Tong, *Adv. Mater.* **2014**, *26*, 3148.

[66] A. El-Habib, M. Addou, A. Aouni, M. Diani, K. Nouneh, J. Zimou, A. Marjaoui, Z. Barbouch, M. Zanouni, Z. El Jouad, *Opt. Mater.* **2022**, *127*, 112312.

[67] J. Wang, Z. Wang, M. Zhang, X. Huo, M. Guo, *Adv. Opt. Mater.* **2024**, *12*, 2302344.

[68] Z. Wang, Q. Zhang, S. Cong, Z. Chen, J. Zhao, M. Yang, Z. Zheng, S. Zneg, X. Yang, F. Genge, Z. Zhao, *Adv. Opt. Mater.* **2017**, *5*, 1700194.

[69] M. Barawi, L. De Trizio, R. Giannuzzi, G. Veramonti, L. Manna, M. Manca, *ACS Nano* **2017**, *11*, 3576.

[70] N. Tran, L. Croguennec, M. Ménétrier, F. Weill, P. Biensan, C. Jordy, C. Delmas, *Chem. Mater.* **2008**, *20*, 4815.

[71] T. Ohsaka, Y. Kanzaki, M. Abe, *Mater. Res. Bull.* **2001**, *36*, 2141.

[72] J. C. Pérez-Flores, C. Baehtz, A. Hoelzel, A. Kuhn, F. García-Alvarado, *RSC Adv.* **2012**, *2*, 3530.

[73] S. Jouanneau, S. Sarciaux, A. Le Gal La Salle, D. Guyomard, *Solid State Ionics* **2001**, *140*, 223.

[74] N. Bondarenko, O. Eriksson, N. V. Skorodumova, *Phys. Rev. B* **2015**, *92*, 165119.

[75] A. Maho, S. Nayak, F. Gillissen, R. Cloots, A. Rougier, *Coatings* **2023**, *13*, 1879.

[76] Y. Kuwahara, Y. Yoshimura, K. Haematsu, H. Yamashita, *J. Am. Chem. Soc.* **2018**, *140*, 9203.

[77] P. Kubelka, F. Munk, *Z. Tech. Phys.* **1931**, *12*, 593.

[78] G. Kortüm, *Reflectance Spectroscopy: Principles, Methods, Applications*, Springer-Verlag, Berlin **1969**.

[79] C. G. Granqvist, *Electrochim. Acta* **1999**, *44*, 3005.